

TREETOP: TOPOLOGY OPTIMIZATION USING CONSTRUCTIVE SOLID GEOMETRY TREES

Rahul Kumar Padhy¹, Pramod Thombre¹, Krishnan Suresh^{1,*}, and Aaditya Chandrasekhar²

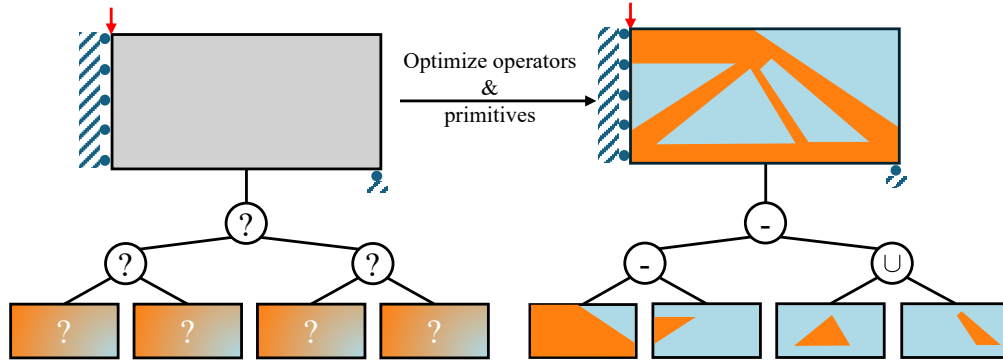
¹Department of Mechanical Engineering, University of Wisconsin-Madison, Madison, WI, USA
{rkpadhy, pthombre, ksuresh}@wisc.edu

²Department of Mechanical Engineering, Northwestern University, Evanston, IL, USA
cs.aaditya@gmail.com

*Corresponding author

ABSTRACT

Feature-mapping methods for topology optimization (FMTO) facilitate direct geometry extraction by leveraging high-level geometric descriptions of the designs. However, FMTO often relies solely on Boolean unions, which can restrict the design space. This work proposes an FMTO framework leveraging an expanded set of Boolean operations, namely, union, intersection, and subtraction. The optimization process entails determining the primitives and the optimal Boolean operation tree. In particular, the framework leverages a recently proposed unified Boolean operation approach. This approach presents a continuous and differentiable function that interpolates the Boolean operations, enabling gradient-based optimization. The proposed methodology is agnostic to the specific primitive parametrization and is showcased through various numerical examples.



Graphical abstract: We perform topology optimization by optimizing the parameters of primitives and the Boolean operations.

Keywords Topology Optimization · Feature Mapping Methods · Constructive Solid Geometry

1 Introduction

Topology optimization (TO) has emerged as a powerful computational tool for achieving optimal material distribution within a design domain, subject to constraints [1, 2]. The maturity of TO methods is evident in their widespread industrial application, particularly facilitated by commercial software.

While various TO methods exist, density-based approaches are widely adopted [2]. Popular density-based approaches discretize the design space into finite elements and optimize a fictitious material density within each element to generate organic, free-form designs [3]. Consider, for instance, the design domain and boundary conditions in fig. 1(a). An optimal design that maximizes stiffness, subject to a volume constraint, using density-based TO is illustrated in fig. 1(b). While offering design freedom, the resulting designs can be challenging to interpret [3, 4] and modify [5]. Furthermore, the density-based TO designs often require extensive post-processing [6] that leads to a deviation between the final design and the optimal solution [7, 8]. This deviation becomes more pronounced when the structure is manufactured using stock material, with components of fixed shape but variable dimensions [8].

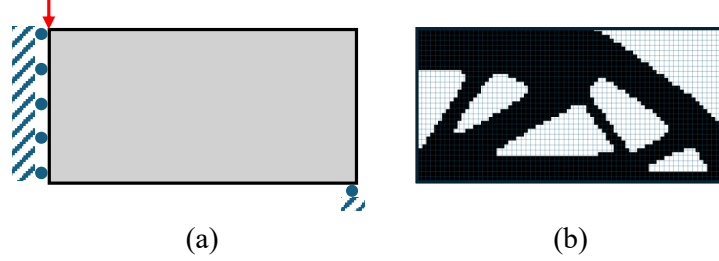


Figure 1: (a) Design domain and boundary conditions. (b) An optimized design obtained through density-based TO.

To address these limitations, alternative techniques, referred to as feature mapping-based topology optimization (FMTO) [3], have emerged. These approaches utilize high-level geometric descriptors (or primitives), to represent the design. For the design domain and boundary conditions illustrated in fig. 2(a), an optimized design obtained using FMTO is presented in fig. 2(b). By parameterizing the design using primitives, FMTO facilitates the upfront enforcement of manufacturing rules, and also aids in design interpretation [3]. However, FMTO methods often rely *solely* on Boolean unions, which can limit design flexibility and fail to exploit the complex geometric operations available in modern computer-aided designing (CAD) systems [3]. While some FMTO methods incorporate Boolean operations other than union, the constructive solid geometry (CSG) tree is typically predefined [9]. The optimization process is then limited to reordering operations or splitting features to introduce new branches [10].

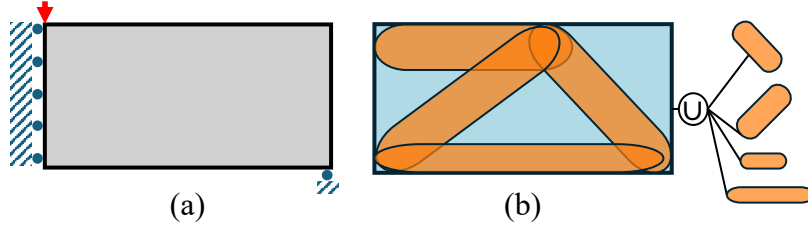


Figure 2: (a) Classic FMTO parameterizes designs using a union of primitives (such as bars).

1.1 Contributions

This work introduces an FMTO framework with the following contributions:

1. **Expanded Boolean Operations:** We extend traditional feature-mapping methods, typically limited to Boolean unions, to incorporate subtraction and intersection operations, significantly expanding the design space. Specifically, we employ a unified Boolean operation formulation [11], where an interpolation function represents various Boolean operations. This formulation enables continuous transitions between different Boolean operations, thus facilitating gradient-based optimization.
2. **Concurrent Optimization:** Unlike prior research [9] that focuses on optimizing only primitive parameters with fixed operators, our framework optimizes both primitive parameters and the Boolean operators simultaneously.

Since we rely on the unified Boolean operation presented in [11], we also inherit the following features:

1. **Mitigating Vanishing Gradients:** The utilization of unified Boolean operations, facilitated by a continuous and monotonic interpolation scheme, enables gradient-based optimization while mitigating the issue of vanishing gradients.
2. **Primitive Parameterization Flexibility:** The proposed method is agnostic to the specific primitive parameterization, accommodating a wide range of geometric primitives.

2 Related Work

As mentioned earlier, FMTO parameterizes the topology via high-level geometric features [12] or primitives that are mapped onto a mesh for analysis [3, 13]. FMTO is driven by the need to integrate features into free-form designs, control specific structural dimensions, utilize stock materials, and generate a geometric representation that can be interpreted by CAD systems [3]. Some of the earliest work in this area combines free-form topology optimization with embedded geometric primitives [14, 15, 16, 17]; for a detailed review, see [3, 18].

We focus on methods that represent the design exclusively using geometric primitives [19, 20, 13, 21]. In particular, we discuss four popular approaches that represent the design as a union of primitives capable of translating, scaling, and modifying their shapes [18]:

1. **Moving morphable components/voids (MMC/MMV) method:** The MMC/MMV method uses geometric primitives, such as B-spline-shaped holes or components, to represent the design [22, 23]. This approach allows for control of the design’s geometry by explicitly manipulating the boundaries of these primitives [24].
2. **Geometry projection (GP) method:** The GP method [25, 20] uses geometric primitives, such as bars [20], supershapes [19, 26] and plates [27], to optimize structural designs by projecting these primitives onto a fixed finite element mesh. This approach has been applied in various contexts, including 3D topology optimization [28], multi-material design [29], and the optimization of unit cells for lattice materials [30].
3. **Method of Moving Morphable Bars (MMB):** The MMB uses round-ended bars as primitives, allowing them to overlap and modify their shape and position within the design [31].
4. **Moving Node Approach (MNA):** Finally, the MNA uses polynomial functions to project geometric primitives, representing the building blocks of the design as mass nodes [32].

The above approaches rely on the Boolean union of primitives [18], which can restrict design flexibility. We propose a generalized framework in (section 3) to enhance design flexibility. Section 3 covers the framework’s key components: primitive parametrization (section 3.2), projection of primitives onto the density field (section 3.3), the use of an expanded set of Boolean operations (union, intersection, subtraction) on the density fields (section 3.4), and optimization strategy (section 3.6). Several examples demonstrating the proposed method are presented in section 4. Finally, section 5 concludes this work.

3 Proposed Method

3.1 Overview

This study focuses on gradient-based topology optimization, which minimizes structural compliance under a volume constraint. We assume that the design domain, loads and restraints, has been prescribed. While the framework is agnostic to the type of primitives used, we will assume that the primitives are polygons for ease of implementation. The CSG tree is assumed to be a perfectly balanced binary tree with a specified depth. Our objective is to obtain an optimal configuration of the polygons at the leaf nodes and Boolean operations at all non-leaf nodes that, when applied, results in the optimized design; see fig. 3.

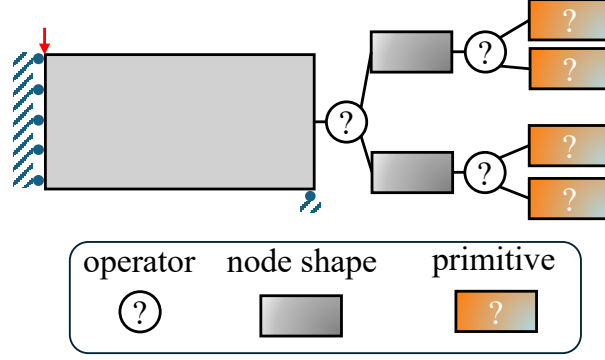


Figure 3: Given a design domain with boundary conditions, the proposed method optimizes the boolean operations (union(\cup), intersection(\cap), difference(\mapsto), and negative difference(\leftarrow)), and the parameters associated with primitives (polygon). The resulting shapes are hierarchically combined till the final design is obtained at the root.

3.2 Primitive Parametrization

We populate the leaf nodes of a perfectly balanced binary CSG with *polygonal* primitives. In particular, a tree with a (given) depth of n_d (discussed in section 4) would correspond to $n_p = 2^{n_d}$ primitives at the leaf nodes. The primitives are parameterized using the method proposed in [33, 13] where:

1. Each polygon primitive $p^{(i)}$ is associated with a reference point $(c_x^{(i)}, c_y^{(i)})$, and is the intersection of S ($S \geq 3$) (straight-line) half-spaces, resulting in a polygon with $\{3, \dots, S\}$ sides; $S = 6$ in fig. 4(a).
2. Each half-space $h_j^{(i)}$ is initially oriented at an angle $\tilde{\alpha}^{(i)} = [0, \pi/3, 2\pi/3, \dots]$ (see fig. 4 (a)) and has an offset distance $d_j^{(i)} > 0$ from the reference point (see fig. 4 (b)).
3. To vary the overall orientation of the polygon, we allow for the rotation of all of its half-spaces by an angle $\theta^{(i)}$, resulting in the final orientation angle $\alpha_j^{(i)} = \theta^{(i)} + \tilde{\alpha}_j^{(i)}$ for the j^{th} half-space (see fig. 4(c)).

In summary, each polygon $p^{(i)}$ is parameterized as:

$$p^{(i)} = \{c_x^{(i)}, c_y^{(i)}, \theta^{(i)}, d_1^{(i)}, \dots, d_S^{(i)}\}, \quad i = 1, \dots, n_p \quad (1)$$

Note that, by construction, each polygon is non-empty and can have between 3 and S sides [13].

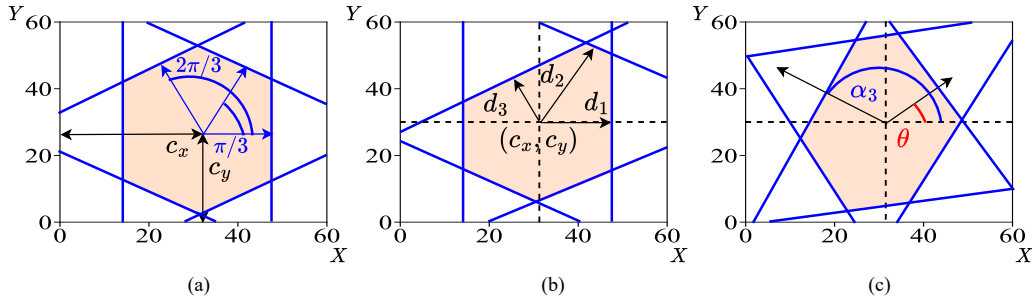


Figure 4: The polygon's parameters include the (a) center coordinates (c_x, c_y) , (b) the distances from the center to the half-spaces (d_1, \dots, d_6) , and (c) an angular offset θ .

3.3 Geometry Projection

The aim of geometry projection is to map primitives, defined by the polygon's parameters (section 3.2) onto a density field defined over a mesh [33]. To maintain differentiability, we first map each primitive (fig. 5(a)) to a signed distance

field (SDF), where the value of the SDF at any point (x, y) is defined as the shortest signed-distance to the primitive’s boundary (inside being negative and outside being positive). We begin by defining the SDF of each half-space as (fig. 5(b)):

$$\hat{\phi}_j^{(i)}(x, y) = (x - c_x^{(i)}) \cos(\alpha_j^{(i)}) + (y - c_y^{(i)}) \sin(\alpha_j^{(i)}) - d_j^{(i)} \quad (2)$$

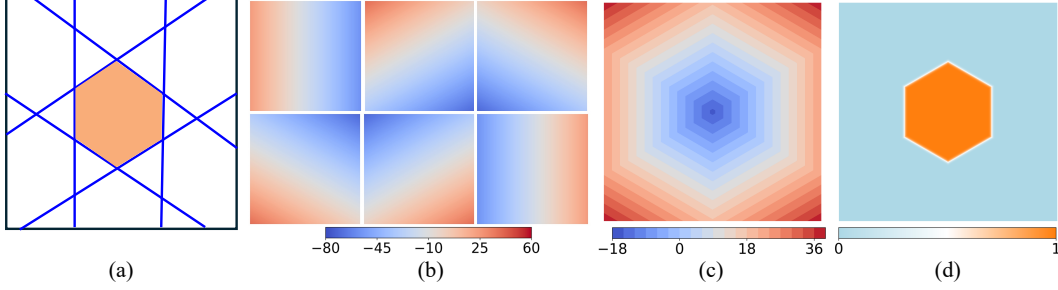


Figure 5: (a) A polygon, (b) signed distance field (SDF) of half-spaces (c) SDF of polygon, and (d) its projected density.

Since the SDF value of a point inside the polygon with respect to a half-space is negative, the SDF of the entire polygon at a given point is obtained by computing the maximum of the SDFs from each half-space at that point (fig. 5(c)). To ensure differentiability, we use the LogSumExp (LSE) approximation of maximum [34]. This yields the SDF of the i^{th} polygon:

$$\phi^{(i)}(x, y) = \frac{l_0}{t} \log \left(\sum_{j=1}^S \exp \left(\frac{t}{l_0} \hat{\phi}_j^{(i)}(x, y) \right) \right) \quad (3)$$

where, t is the LSE scaling factor (discussed later in section 4) and l_0 is the length of the diagonal of the domain bounding box.

Next, we compute the density field of the polygon $\tilde{\rho}(\cdot)$, from $\phi(\cdot)$ using the Sigmoid function; see fig. 5(d):

$$\tilde{\rho}^{(i)}(x, y) = \frac{1}{1 + \exp(-\frac{\gamma}{l_0} \phi^{(i)}(x, y))} \quad (4)$$

Observe that negative SDF values (representing the polygon’s interior) are mapped to a density of one (solid), while positive values (representing the polygon’s exterior) are mapped to zero (void). SDF values near zero (representing the polygon’s boundary), are projected to intermediate density values $\tilde{\rho} \in (0, 1)$, with the sharpness of transition controlled by the hyperparameter γ .

Finally, we impose a threshold filter on $\tilde{\rho}$ to drive intermediate densities towards 1/0 as [35]:

$$\rho(\tilde{\rho}) = \frac{\tanh(\frac{\beta}{2}) + \tanh(\beta(\tilde{\rho} - \frac{1}{2}))}{2 \tanh(\frac{\beta}{2})} \quad (5)$$

where the parameter β controls the sharpness of the threshold function. The obtained primitive densities are subsequently combined using the Boolean operations (as detailed in the following section) to obtain the design density.

3.4 Unified Boolean Operations

The final design density is obtained by applying Boolean operators (fig. 6) to the primitive density fields (operands) defined in the previous section. A successful Boolean operations approach suitable for gradient-based optimization (section 3.6) should possess the following properties:

1. Differentiability with respect to operands (density fields).
2. Differentiability with respect to the Boolean operators (union (\cup), intersection (\cap), difference (\mapsto), negative difference (\mapsto); see fig. 6).

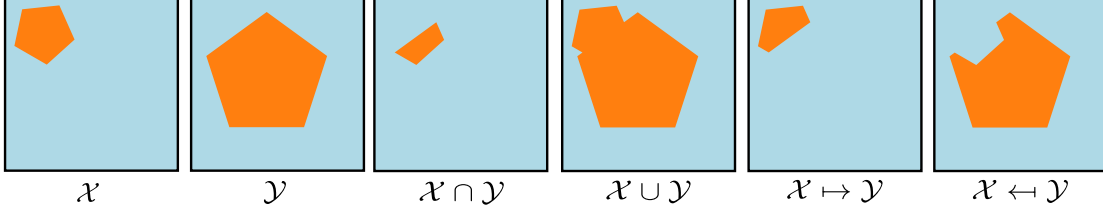


Figure 6: Boolean operators (union (\cup), intersection(\cap), difference(\mapsto), negative difference(\mapleftarrow)) defined over the density fields of two pentagonal primitives.

FMT0 methods that demonstrate differentiability with respect to the operands [20] have been extensively employed. Further, the union and intersection operators are often approximated using smooth maximum/minimum functions [20, 3, 36]. Alternative techniques, such as the smooth blending operator [37] and R-functions [38, 39], have been proposed, exhibiting differentiability with respect to the operands and individual operators. However, a smooth transition between the operators is difficult to achieve. Furthermore, while a unified Boolean approach based on the modified R-function [40] was introduced to facilitate differentiable transitions between operators, it failed to satisfy key Boolean operator axioms, resulting in unexpected behavior [11].

To address these issues, we adopt a unified Boolean operation approach proposed in [11]. Let \mathcal{X} and \mathcal{Y} represent two primitives (polygons), with their corresponding density functions ρ_x and ρ_y . Then, a generalized Boolean operation between the two primitives is defined as (fig. 6):

$$\mathcal{B}(\rho_x, \rho_y; \mathbf{b}) = (b_1 + b_2)\rho_x + (b_1 + b_3)\rho_y + (b_0 - b_1 - b_2 - b_3)\rho_x\rho_y \quad (6)$$

where $\mathbf{b} = \{b_0, b_1, b_2, b_3\}$ are interpolating parameters. The interpolating parameters are constrained by $0 \leq b_i \leq 1$ and $\sum_{i=0}^3 b_i = 1$. When \mathbf{b} is a one-hot vector, we recover the standard Boolean operators (table 1):

Table 1: Boolean operations

\mathbf{b}	Operation	$\mathcal{B}(\rho_x, \rho_y)$
1, 0, 0, 0	$\mathcal{X} \cap \mathcal{Y}$	$\rho_x \rho_y$
0, 1, 0, 0	$\mathcal{X} \cup \mathcal{Y}$	$\rho_x + \rho_y - \rho_x \rho_y$
0, 0, 1, 0	$\mathcal{X} \mapsto \mathcal{Y}$	$\rho_x - \rho_x \rho_y$
0, 0, 0, 1	$\mathcal{X} \mapleftarrow \mathcal{Y}$	$\rho_y - \rho_x \rho_y$

Observe that eq. (6) continuously interpolates between individual operators. For the two polygons in fig. 6, the continuous interpolation between the intersection and union operators is illustrated in fig. 7, while a generic operator state is illustrated in fig. 8.

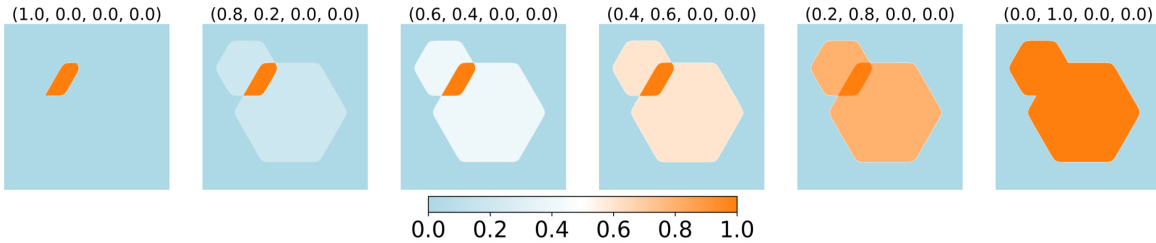


Figure 7: Continuous interpolation between intersection (\cap) and union (\cup).

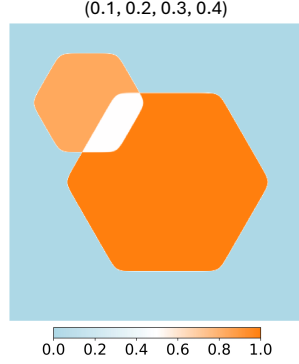


Figure 8: The Boolean operand b with intermediate non-zero values and the resulting density field.

Furthermore, the function \mathcal{B} is differentiable with respect to both the operands (ρ_x, ρ_y) and the operators (b_i) . For example, the derivative w.r.t operand ρ_x is:

$$\frac{\partial \mathcal{B}}{\partial \rho_x} = (b_1 + b_2) + (b_0 - b_1 - b_2 - b_3)\rho_y \quad (7)$$

while the derivative with respect to operator coefficient b_1 is

$$\frac{\partial \mathcal{B}}{\partial b_1} = \rho_x + \rho_y - \rho_x \rho_y \quad (8)$$

Finally, with the interpolated operators defined at all non-leaf nodes and the primitive densities at the leaf nodes, we can evaluate the CSG tree bottom-up to obtain the density field $\rho(x, y)$ of the evolving design at any instance.

3.5 Finite element analysis

For finite element analysis, we use here a structured mesh with bilinear quad elements. Having obtained the design density field $\rho(x, y)$, let ρ_e be the density at the center of element e . The corresponding Young's modulus E_e is obtained using the Solid Isotropic Material Penalization (SIMP) model [2] as:

$$E_e = E_{min} + (E_0 - E_{min})(\rho_e)^p \quad (9)$$

where E_0 is Young's modulus of the solid material, E_{min} is a small constant added to prevent a singular global stiffness matrix, and p is the SIMP penalty. One can evaluate the element stiffness matrix as

$$[K_e] = E_e \int_{\Omega_e} [B]^T [D_0] [B] d\Omega_e \quad (10)$$

where $[B]$ is the strain matrix, and $[D_0]$ is the constitutive matrix with a Young's modulus of unity and an assumed Poisson's ratio (see Table 2). This is followed by the assembly of the global stiffness matrix \mathbf{K} . Finally, with the imposed nodal force vector \mathbf{f} , we solve the state equation for the nodal displacements $\mathbf{u} = \mathbf{K}^{-1} \mathbf{f}$.

3.6 Optimization

We now summarize various aspects of the optimization problem:

Objective: We consider here a compliance minimization problem. where the compliance is computed as $J = \mathbf{f}^T \mathbf{u}$.

Volume constraint: The design is subjected to a total volume constraint. With v_f^* being the maximum allowed volume fraction and v_e being the element areas, the volume constraint g_v is defined as:

$$g_v \equiv \frac{\sum_{e=1}^{N_e} \rho(\mathbf{x}_e) v_e}{v_f^* \sum_{e=1}^{N_e} v_e} - 1 \leq 0 \quad (11)$$

Optimization variables: The optimization variables are as follows:

1. Recall that the design is defined by polygon parameters, including center coordinates, angular offset, and plane distances, resulting in $n_p(S + 3)$ free parameters (see Section 3.2). Additionally, the design requires $n_b = 2^{n_d} - 1$ boolean operations ($\vec{\mathbf{b}} = \mathbf{b}^{(1)}, \dots, \mathbf{b}^{(n_b)}$) for a tree of depth n_d .
2. For optimization, we define an augmented normalized design vector $\mathbf{z} = [\mathbf{z}_{c_x}, \mathbf{z}_{c_y}, \mathbf{z}_\theta, \mathbf{z}_d, \mathbf{z}_b]$ that lie in $[0, 1]$. With $\underline{c}_x, \underline{c}_y, \underline{\theta}, \underline{d}$ being the lower bound and $\bar{c}_x, \bar{c}_y, \bar{\theta}, \bar{d}$ being the upper bound on the parameters of the polygons, we can retrieve the unnormalized x-center as $\mathbf{c}_x \leftarrow \underline{c}_x + (\bar{c}_x - \underline{c}_x) \mathbf{z}_{c_x}$ and so on. The design variable $\mathbf{z}_b^{(i)}$, corresponding to the i^{th} boolean operator is transformed into one-hot encoding using a softmax function [11].
3. All design variables \mathbf{z} are uniform-randomly initialized (using numpy) with a default seed value of 2.

TO problem: The final TO problem is posed as:

$$\underset{\mathbf{z}}{\text{minimize}} \quad J = \mathbf{f}^T \mathbf{u}(\mathbf{z}) \quad (12a)$$

$$\text{subject to} \quad \mathbf{K}(\mathbf{z}) \mathbf{u} = \mathbf{f} \quad (12b)$$

$$g_v(\mathbf{z}) \leq 0 \quad (12c)$$

$$0 \leq z_i \leq 1 \quad \forall i \quad (12d)$$

Optimization method: We employ the method of moving asymptotes (MMA) [41] to perform the design updates. Specifically, we use a Python implementation with all default parameters corresponding to the version of MMA presented in [42]. The choices of the MMA move limit, the step tolerance, the Karush-Kuhn-Tucker (KKT) tolerances, etc are specified later under numerical experiments.

3.7 Sensitivity Analysis

Sensitivity computation, a crucial aspect of gradient-based optimization, involves determining the derivatives of the objective function and constraints with respect to the optimization parameters. Traditionally, this is conducted manually, which can be labor-intensive and error-prone. However, by utilizing the automatic differentiation (AD) [43, 44] capabilities of frameworks such as JAX [45], this step can be fully automated, ensuring accurate and efficient computation. In practical terms, we only need to define the forward expressions, and the derivatives of the objective and volume constraint with respect to the optimization variables is automatically computed with machine precision. Finally, we summarize the algorithm for the proposed framework in fig. 9.

4 Numerical Experiments

In this section, we conduct several experiments to illustrate the proposed framework. The default parameters in the experiments are summarized in Table 2. All experiments are conducted on a MacBook M2 Air, using the JAX library [45] in Python. Additionally, all design parameters \mathbf{z} are uniform randomly initialized.

4.1 Validation

We compare the designs from our proposed framework with those obtained using the SIMP-based optimization [46]. Using the default parameters outlined in table 2, and with $n_d = 4$, we optimize both the Boolean operators and polygon parameters for an MBB beam (fig. 10(a)). In the SIMP implementation, the density field is optimized with a filtering radius of 1.3, targeting a volume fraction of $v_f^* = 0.5$ (fig. 10(b)). For the proposed method, we display the final design in fig. 10(c). We observe that both methods yield similar designs and performance. For illustration, we present the complete resulting CSG tree in fig. 11.

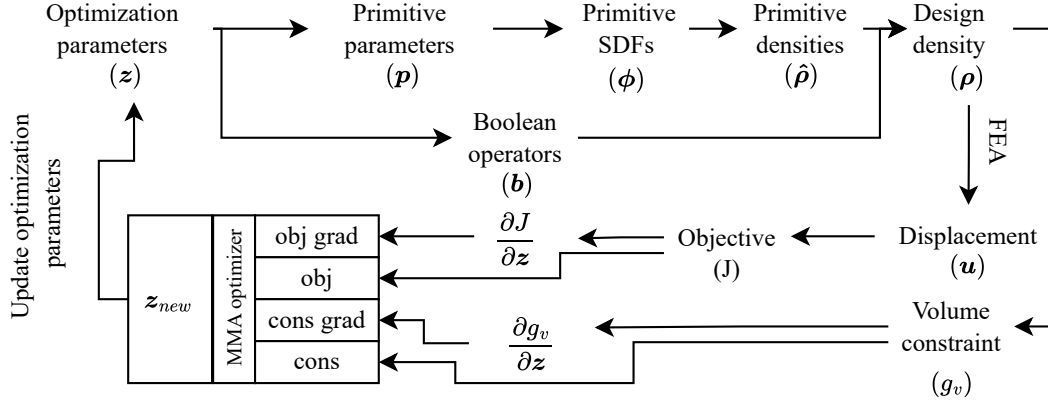


Figure 9: Optimization loop of the proposed framework.

Table 2: Default parameters

Parameter	Description and default value
E_0, ν	$E_0 = 1$ and Poisson's ratio $\nu = 0.3$
n_e	Number of FEA mesh elements of (60×30)
l_x, l_y	Length of domain $(60, 30)$ along x and y
S	Sides of polygon = 6
$(\underline{c}_x, \bar{c}_x)$	Polygon x-center range $(0.05l_x, 0.95l_x)$
$(\underline{c}_y, \bar{c}_y)$	Polygon y-center range $(0.05l_y, 0.95l_y)$
\underline{d}, \bar{d}	Polygon face offset range $(0, 0.25l_x)$
γ	Sharpness param in density projection = 100
β	Sharpness param in threshold filter = 8
t	Scaling factor of the LSE function = 100
seed	Random seed for initialization = 2
maxIter	Max number of optim iters = 200
move limit	MMA step size = 0.05
kkt tolerance	MMA convergence criteria = 10^{-3}
step tolerance	MMA convergence criteria = 10^{-3}

Additionally, the convergence is illustrated in fig. 12. The resulting density fields at the root nodes for the 10th, 50th, 75th, and final (111th) iterations are shown as insets. In comparison, the SIMP-based implementation took 126 iterations to converge. In our framework, the percentage of computational time is as follows: 0.6% for geometry projection, 8.1% for CSG tree evaluation, and 91.3% for FEA and sensitivity analysis; each iteration takes 1.6 seconds.

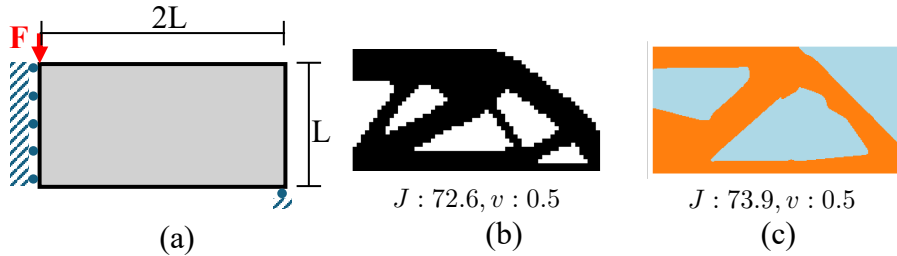


Figure 10: Validation: (a) MBB problem, (b) SIMP generated topology, and (c) design from the proposed framework.

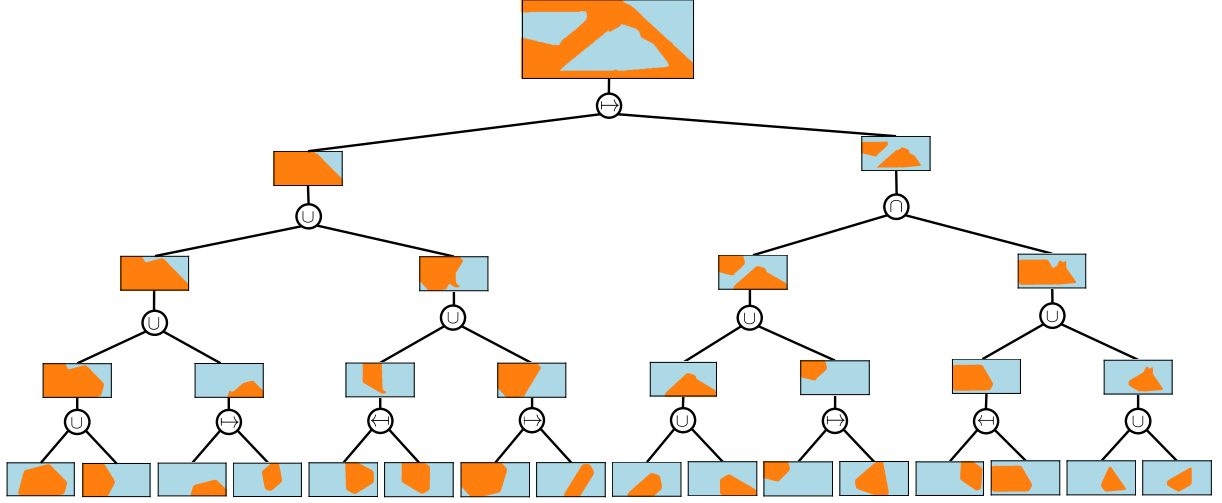


Figure 11: CSG tree with $n_d = 4$. $J = 72.3$ with $v_f^* = 0.5$.

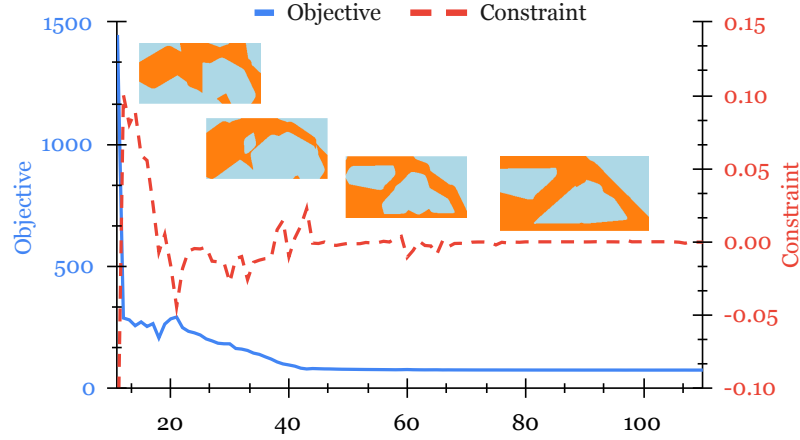
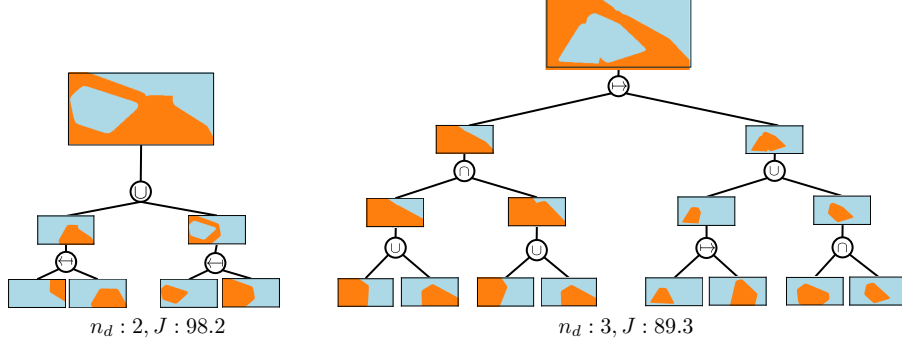
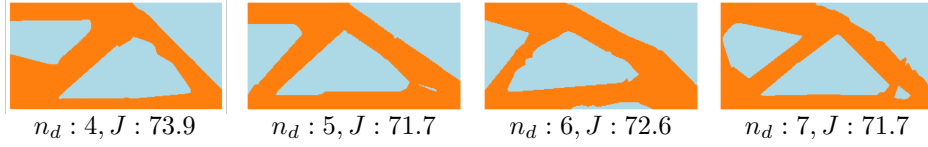


Figure 12: Convergence of the objective and constraint for an MBB beam with $v_f^* = 0.5$.

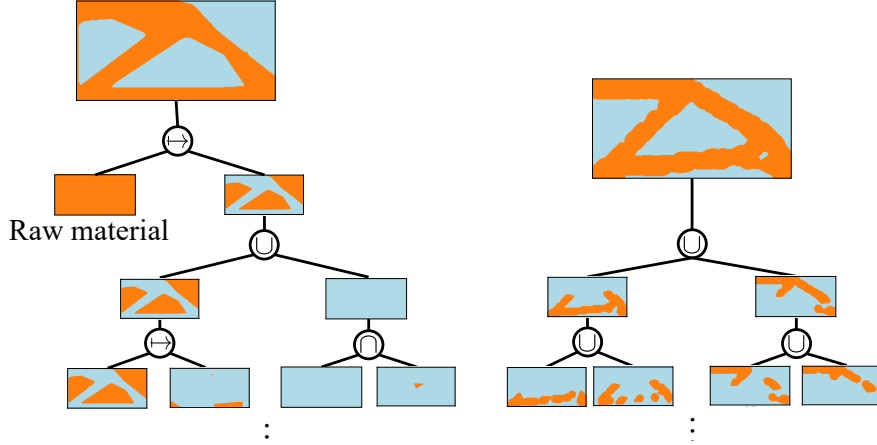
4.2 Effect of Tree Depth

In this experiment, we examine the effect of the CSG tree depth n_d on the performance of the design. We revisit the MBB beam in fig. 10(a), with $v_f^* = 0.5$, and investigate the impact of different values of n_d . The CSG tree for $n_d = 2$ and $n_d = 3$ are illustrated in fig. 13, while the final designs for $n_d = 4, 5, 6, 7$ are illustrated in fig. 14. The performance improves as n_d increases; no significant improvements were observed beyond the depth of $n_d = 4$. Based on similar experiments, we recommend using a depth $n_d \geq 4$; we use a depth of $n_d = 6$ for the remainder of the experiments.

Figure 13: CSG tree with $n_d = 2$ and $n_d = 3$ with $v_f^* = 0.5$.Figure 14: The final designs and compliances with $n_d = 4, 5, 6, 7$.

4.3 Flexibility of Framework

In this experiment, we demonstrate the framework’s ability to obtain optimal designs with specific Boolean structures. We again consider the MBB problem (fig. 10(a)) with $v_f^* = 0.5$. First, we set the root node operator as a difference operator, resulting in the design shown in fig. 15(a). Observe that the optimization can sometimes result in empty nodes. These nodes and their descendants are detected and pruned [47]. Next, we only allowed union operators; the resulting topology is illustrated in fig. 15(b).

Figure 15: (a) Difference operator at the root, $J = 79.3$. (b) Only unions operators allowed, $J = 74.9$.

4.4 Mesh dependency

Next, we study the effect of the FE mesh on the computed topology using the MBB problem with $v_f^* = 0.5$ (fig. 10(a)), while keeping all other parameters at their default values. Figure 16 presents the topologies for varying mesh sizes: 60×30 , 80×40 , and 100×50 elements. No significant difference in performance was observed across these mesh sizes. However, we note that the designs exhibit less noise as the number of mesh elements increases. The boundary exhibits small features for a coarse mesh, since the latter fails to capture the impact of small features on the performance. However, we have observed that these undesirable features tend to reduce as the mesh size increases.



Figure 16: Dependency on mesh size: (a) 60×30 , $J = 72.6$. (b) 80×40 , $J = 73.1$. (c) 100×50 , $J = 75.9$.

4.5 Effect of Initialization

Recall all design variables z are uniform-randomly initialized with a default seed value of 2. We now investigate the influence of the seed value on the optimal designs. While all topology optimization techniques are inherently sensitive to the initial design [48], it has been observed that this dependency is particularly pronounced in feature-mapping techniques [27]. In this specific example, we consider the design of an MBB beam (fig. 10(a)) with 100×50 mesh elements. The resulting designs and their corresponding performances for various initial seeds are compared in fig. 17. Observe that while we obtain diverse designs, the performances are similar. This suggests that, as expected, the landscape is highly non-convex with numerous local solutions.

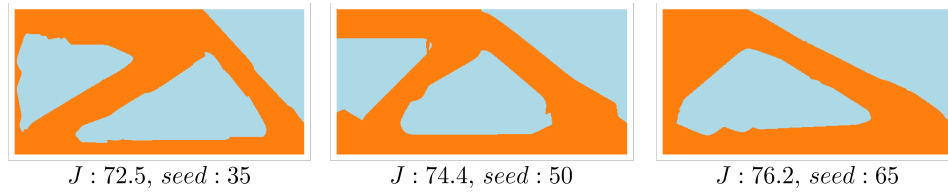


Figure 17: Dependency on initialization.

4.6 Pareto

An essential consideration during the design phase is the exploration of the Pareto front; evaluating the trade-offs associated with various design choices. Let us consider the mid cantilever beam problem illustrated in fig. 18(a). With 100×50 mesh elements, $n_d = 6$ and $S = 6$, we investigate the trade-off between the structure's compliance and volume fraction. fig. 18(b) illustrates the resulting designs (and the intermediate densities at the first depth) at various volume fractions. As anticipated, we observe an increase in compliance as the allowable volume fraction is decreased. We did not impose explicit symmetry requirements on the CSG tree.

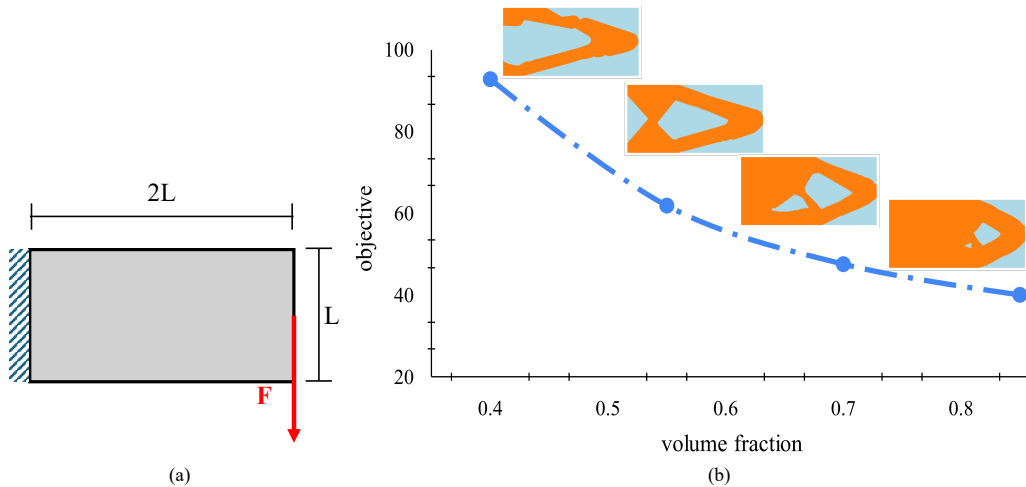


Figure 18: Trade-off between compliance and volume.

5 Conclusion

We introduce an FMTO framework that concurrently optimizes both the primitive parameters and the Boolean operators (union, intersection, and subtraction). Notably, by leveraging a unified Boolean operation approach, the framework improves upon existing FMTO methods that typically rely on predefined CSG trees and/or are limited to optimizing only primitive parameters operated with unions. The efficacy of the proposed method was demonstrated through various numerical examples.

The generated tree structure appears unnatural and dissimilar to human-designed trees. This presents an opportunity to combine the proposed method with machine learning-based frameworks [49, 50] to mimic human-designed CSG trees. The method also suffers from some of the shortcomings inherent to FMTO methods. For example, the optimizer is highly susceptible to being trapped in local optima; it is also sensitive to initialization. Additionally, the optimizer may fail to converge to an optimal solution when fewer primitives are used [3].

Nevertheless, several avenues for future research remain. For instance, manufacturing constraints such as symmetry, feature size control must be incorporated. One promising direction is to incorporate CNC operations into the TO process, ensuring that designs are both optimal and manufacturable [51]. Further, optimizing the primitive type and depth of the tree in conjunction with the operators and primitive parameters requires investigation [36, 52].

Acknowledgments

The University of Wisconsin, Madison Graduate School supported this work.

Compliance with ethical standards

The authors declare that they have no conflict of interest.

Replication of Results

The Python code is available at [github.com//UW-ERSL/TreeTOP](https://github.com/UW-ERSL/TreeTOP)

References

- [1] Martin Philip Bendsoe and Ole Sigmund. *Topology optimization: theory, methods, and applications*. Springer Science & Business Media, 2013.
- [2] Ole Sigmund and Kurt Maute. Topology optimization approaches: A comparative review. *Structural and multidisciplinary optimization*, 48(6):1031–1055, 2013.
- [3] Fabian Wein, Peter D Dunning, and Julián A Norato. A review on feature-mapping methods for structural optimization. *Structural and multidisciplinary optimization*, 62:1597–1638, 2020.
- [4] Daxuan Ren, Jianmin Zheng, Jianfei Cai, Jiatong Li, Haiyong Jiang, Zhongang Cai, Junzhe Zhang, Liang Pan, Mingyuan Zhang, Haiyu Zhao, et al. Csg-stump: A learning friendly csg-like representation for interpretable shape parsing. In *Proceedings of the IEEE/CVF international conference on computer vision*, pages 12478–12487, 2021.
- [5] Constructive Solid Geometry. Neural shape parsers for constructive solid geometry. *IEEE Transactions on Pattern Analysis and Machine Intelligence*, 44(5), 2022.
- [6] Subodh C Subedi, Chaman Singh Verma, and Krishnan Suresh. A review of methods for the geometric post-processing of topology optimized models. *Journal of Computing and Information Science in Engineering*, 20(6):060801, 2020.
- [7] Benliang Zhu, Xianmin Zhang, Hongchuan Zhang, Junwen Liang, Haoyan Zang, Hai Li, and Rixin Wang. Design of compliant mechanisms using continuum topology optimization: A review. *Mechanism and Machine Theory*, 143:103622, 2020.
- [8] Shanglong Zhang, Arun L Gain, and Julián A Norato. Adaptive mesh refinement for topology optimization with discrete geometric components. *Computer Methods in Applied Mechanics and Engineering*, 364:112930, 2020.
- [9] Ying Zhou, Weihong Zhang, Jihong Zhu, and Zhao Xu. Feature-driven topology optimization method with signed distance function. *Computer Methods in Applied Mechanics and Engineering*, 310:1–32, 2016.

- [10] Jikai Liu and Albert C To. Computer-aided design-based topology optimization system with dynamic feature shape and modeling history evolution. *Journal of Mechanical Design*, 142(7):071704, 2020.
- [11] Hsueh-Ti Derek Liu, Maneesh Agrawala, Cem Yuksel, Tim Omernick, Vinith Misra, Stefano Corazza, Morgan McGuire, and Victor Zordan. A unified differentiable boolean operator with fuzzy logic. In *ACM SIGGRAPH 2024 Conference Papers*, pages 1–9, 2024.
- [12] Vadim Shapiro. Solid modeling. *Handbook of computer aided geometric design*, 20:473–518, 2002.
- [13] Aaditya Chandrasekhar. PolyTO: Structural topology optimization using convex polygons. *arXiv preprint arXiv:2305.04406*, 2023.
- [14] Zhongyan Qian and GK Ananthasuresh. Optimal embedding of rigid objects in the topology design of structures. *Mechanics Based Design of Structures and Machines*, 32(2):165–193, 2004.
- [15] Jiaqin Chen, Vadim Shapiro, Krishnan Suresh, and Igor Tsukanov. Parametric and topological control in shape optimization. In *International Design Engineering Technical Conferences and Computers and Information in Engineering Conference*, volume 4255, pages 575–586, 2006.
- [16] Liang Xia, Jihong Zhu, and Weihong Zhang. Sensitivity analysis with the modified heaviside function for the optimal layout design of multi-component systems. *Computer methods in applied mechanics and engineering*, 241:142–154, 2012.
- [17] Zhan Kang, Yaguang Wang, and Yiqiang Wang. Structural topology optimization with minimum distance control of multiphase embedded components by level set method. *Computer Methods in Applied Mechanics and Engineering*, 306:299–318, 2016.
- [18] Simone Coniglio, Joseph Morlier, Christian Gogu, and Rémi Amargier. Generalized geometry projection: a unified approach for geometric feature based topology optimization. *Archives of Computational Methods in Engineering*, 27:1573–1610, 2020.
- [19] Julián A Norato. Topology optimization with supershapes. *Structural and Multidisciplinary Optimization*, 58(2):415–434, 2018.
- [20] JA Norato, BK Bell, and Daniel A Tortorelli. A geometry projection method for continuum-based topology optimization with discrete elements. *Computer Methods in Applied Mechanics and Engineering*, 293:306–327, 2015.
- [21] Rahul Kumar Padhy and Aaditya Chandrasekhar. PhoTOS: Topology optimization of photonic components using a shape library. *arXiv preprint arXiv:2407.00845*, 2024.
- [22] Xu Guo, Weisheng Zhang, Jian Zhang, and Jie Yuan. Explicit structural topology optimization based on moving morphable components (mmc) with curved skeletons. *Computer methods in applied mechanics and engineering*, 310:711–748, 2016.
- [23] Weisheng Zhang, Jishun Chen, Xuefeng Zhu, Jianhua Zhou, Dingchuan Xue, Xin Lei, and Xu Guo. Explicit three dimensional topology optimization via moving morphable void (mmv) approach. *Computer Methods in Applied Mechanics and Engineering*, 322:590–614, 2017.
- [24] Weisheng Zhang, Wanying Yang, Jianhua Zhou, Dong Li, and Xu Guo. Structural topology optimization through explicit boundary evolution. *Journal of Applied Mechanics*, 84(1):011011, 2017.
- [25] Bryan Bell, Julian Norato, and Daniel Tortorelli. A geometry projection method for continuum-based topology optimization of structures. In *12th AIAA Aviation Technology, integration, and operations (ATIO) conference and 14th AIAA/ISSMO multidisciplinary analysis and optimization conference*, page 5485, 2012.
- [26] Rahul Kumar Padhy, Krishnan Suresh, and Aaditya Chandrasekhar. TOMAS: topology optimization of multiscale fluid flow devices using variational auto-encoders and super-shapes. *Structural and Multidisciplinary Optimization*, 67(7):119, 2024.
- [27] Shanglong Zhang, Julián A Norato, Arun L Gain, and Naesung Lyu. A geometry projection method for the topology optimization of plate structures. *Structural and Multidisciplinary Optimization*, 54:1173–1190, 2016.
- [28] Shanglong Zhang, Arun L Gain, and Julián A Norato. A geometry projection method for the topology optimization of curved plate structures with placement bounds. *International Journal for Numerical Methods in Engineering*, 114(2):128–146, 2018.
- [29] Hesaneh Kazemi, Ashkan Vaziri, and Julián A Norato. Topology optimization of structures made of discrete geometric components with different materials. *Journal of Mechanical Design*, 140(11):111401, 2018.
- [30] Seth Watts and Daniel A Tortorelli. A geometric projection method for designing three-dimensional open lattices with inverse homogenization. *International Journal for Numerical Methods in Engineering*, 112(11):1564–1588, 2017.

- [31] Van-Nam Hoang and Gang-Won Jang. Topology optimization using moving morphable bars for versatile thickness control. *Computer Methods in Applied Mechanics and Engineering*, 317:153–173, 2017.
- [32] Johannes TB Overvelde. The moving node approach in topology optimization. 2012.
- [33] Boyang Deng, Kyle Genova, Soroosh Yazdani, Sofien Bouaziz, Geoffrey Hinton, and Andrea Tagliasacchi. Cvxnet: Learnable convex decomposition. In *Proceedings of the IEEE/CVF Conference on Computer Vision and Pattern Recognition*, pages 31–44, 2020.
- [34] Aston Zhang, Zachary C Lipton, Mu Li, and Alexander J Smola. Dive into deep learning. *arXiv preprint arXiv:2106.11342*, 2021.
- [35] Jun Wu, Niels Aage, Rüdiger Westermann, and Ole Sigmund. Infill optimization for additive manufacturing—approaching bone-like porous structures. *IEEE transactions on visualization and computer graphics*, 24(2):1127–1140, 2017.
- [36] Fenggen Yu, Zhiqin Chen, Manyi Li, Aditya Sanghi, Hooman Shayani, Ali Mahdavi-Amiri, and Hao Zhang. Capri-net: Learning compact cad shapes with adaptive primitive assembly. In *Proceedings of the IEEE/CVF Conference on Computer Vision and Pattern Recognition*, pages 11768–11778, 2022.
- [37] Antonio Ricci. A constructive geometry for computer graphics. *The Computer Journal*, 16(2):157–160, 1973.
- [38] VL Rvachev. On the analytical description of some geometric objects”, reports of ukrainian academy of sciences, vol. 153, no. 4, 765–767, 1963.
- [39] Vadim Shapiro. Semi-analytic geometry with r-functions. *ACTA numerica*, 16:239–303, 2007.
- [40] Brian Wyvill, Andrew Guy, and Eric Galin. Extending the csg tree. warping, blending and boolean operations in an implicit surface modeling system. In *Computer Graphics Forum*, volume 18, pages 149–158. Wiley Online Library, 1999.
- [41] Krister Svanberg. The method of moving asymptotes—a new method for structural optimization. *International journal for numerical methods in engineering*, 24(2):359–373, 1987.
- [42] Krister Svanberg. Mma and gmma-two methods for nonlinear optimization. *vol*, 1:1–15, 2007.
- [43] Aaditya Chandrasekhar, Saketh Sridhara, and Krishnan Suresh. AuTO: a framework for automatic differentiation in topology optimization. *Structural and Multidisciplinary Optimization*, 64(6):4355–4365, 2021.
- [44] Momchil Minkov, Ian AD Williamson, Lucio C Andreani, Dario Gerace, Beicheng Lou, Alex Y Song, Tyler W Hughes, and Shanhui Fan. Inverse design of photonic crystals through automatic differentiation. *Acs Photonics*, 7(7):1729–1741, 2020.
- [45] James Bradbury, Roy Frostig, Peter Hawkins, Matthew James Johnson, Chris Leary, Dougal Maclaurin, George Neca, Adam Paszke, Jake VanderPlas, Skye Wanderman-Milne, and Qiao Zhang. JAX: composable transformations of Python+NumPy programs, 2018.
- [46] Erik Andreassen, Anders Clausen, Mattias Schevenels, Boyan S Lazarov, and Ole Sigmund. Efficient topology optimization in matlab using 88 lines of code. *Structural and Multidisciplinary Optimization*, 43:1–16, 2011.
- [47] Robert B Tilove. A null-object detection algorithm for constructive solid geometry. *Communications of the ACM*, 27(7):684–694, 1984.
- [48] Suna Yan, Fengwen Wang, and Ole Sigmund. On the non-optimality of tree structures for heat conduction. *International Journal of Heat and Mass Transfer*, 122:660–680, 2018.
- [49] Sebastian Koch, Albert Matveev, Zhongshi Jiang, Francis Williams, Alexey Artemov, Evgeny Burnaev, Marc Alexa, Denis Zorin, and Daniele Panozzo. ABC: A big cad model dataset for geometric deep learning. In *The IEEE Conference on Computer Vision and Pattern Recognition (CVPR)*, June 2019.
- [50] Pu Li, Jianwei Guo, Xiaopeng Zhang, and Dong-Ming Yan. Secad-net: Self-supervised cad reconstruction by learning sketch-extrude operations. In *Proceedings of the IEEE/CVF Conference on Computer Vision and Pattern Recognition*, pages 16816–16826, 2023.
- [51] Mohsen Yavartanoo, Sangmin Hong, Reyhaneh Neshatavar, and Kyoung Mu Lee. CNC-Net: Self-supervised learning for cnc machining operations. In *Proceedings of the IEEE/CVF Conference on Computer Vision and Pattern Recognition*, pages 9816–9825, 2024.
- [52] Fenggen Yu, Qimin Chen, Maham Tanveer, Ali Mahdavi Amiri, and Hao Zhang. D^2 CSG: Unsupervised learning of compact csg trees with dual complements and dropouts. *Advances in Neural Information Processing Systems*, 36, 2024.